Breast Cancer Diagnosis with Machine Learning Using Feed-Forward Multilayer Perceptron Analog Artificial Neural Network

Djimeli-Tsajio Alain B.[1], Koagne Longpa T. Silas[2,*], Lienou T. Jean-Pierre[3], Noulamo Thierry[3], and Geh Wilson Ejuh[4,5]
[1] Department of Telecom. and Network Engineering, IUT-FV, University of Dschang, Bandjoun, Cameroon
[2] Research Unit of Automation and Applied Computer Science URAIA, IUT-FV, University of Dschang, Bandjoun, Cameroon
[3] Department of Computer Engineering, IUT-FV, University of Dschang, Bandjoun, Cameroon
[4] Department of General and Scientific Studies, IUT-FV, University of Dschang, Bandjoun, Cameroon
[5] Department of Electri. and Electro. Eng., NAHPI, University of Bamenda, Bambili, Cameroon
Email: alain.djimeli@univ-dschang.org (D.T.A.B.), silas.koagne@univ-dschang.org (K.L.T.S.), Jp.lienou@univ-dschang.org (L.T.J.-P.), thierry.noulamo@univ-dschang.org (N.T.), gehwilsonejuh@yahoo.fr (G.W.E.)

***Abstract*—An analog network classifier based on a multiplier and non-linear functions is presented in this paper, executing binary classification on breast cancer cells, and categorizing biopsies as benign or malignant tumors. An off-chip learning on-chip inference methodology is proposed for implementing a feed-forward analog artificial neural network based on fundamental design analog block circuits, realized with the aid of 90 nm CMOS technology. These circuits are meticulously designed and fine-tuned at the transistor scale to meet design criteria while minimizing power consumption. Through Spice simulations, the basic analog blocks were developed, leading to the specification of the full-chip hardware neural network. The Monte Carlo analysis of the final circuit reveals that the network achieves 96.85% accuracy and 0.9309 MCC on the Wisconsin breast cancer dataset, with a power consumption of 31.95 µW, and power supply rail of ±900 mV per analog circuit component and computational unit. The model effectively captures data patterns, providing stable, reliable, and robust predictions.**

***Index Terms*—Analog artificial neural network, very large-scale integration, complementary metal-oxide semiconductor, breast cancer classification, multilayer perceptron**

I. Introduction

Breast cancer remains one of the most common cancers and the leading cause of mortality among women worldwide. This spotlights the urgent need for early and efficient diagnostic methods. Over the past ten years, the use of Artificial Neural Networks (ANN) has developed in many disciplines [1]. They are particularly applied for classification, prediction, optimization, and associative memory [2–4]. ANN resulted from the admiration of how the human brain computes complex processes, which is entirely different from the way conventional digital computers do this [5]. Drawing their inspiration from research on human brain functioning, ANNs are capable of learning from experience.

An ANN is defined as an information processing system inspired by the functioning of the human brain to learn [6]. On the other hand, an analog implementation simply refers to the design and realization of a system using electronic components. Thus, the implementation of an Analog Artificial Neural Network (AANN) is then referred to as the design and realization of an information processing system inspired by the functioning of the human brain to learn using electronic components.

ANNs are particularly attractive for Complementary Metal-Oxide Semiconductor (CMOS) Very Large-Scale Integration (VLSI) implementations because each parallel element (that is, neuron or synapse) is relatively realized with the aid of electronic components, allowing the complete integration of large networks on a single chip [7, 8]. Multipliers, nonlinear functions (also called activation functions), and their derivatives are key elements in an Analog Very Large-Scale Integration (AVLSI) implementation of ANNs [9].

Breast cancer cells classification as malignant or benign tumors was chosen for the verification of this work. Hence, it will be necessary to find the best compromises of obtained analog structures through simulations in Cadence Virtuoso for achieving optimized circuits in mature 90 nm CMOS technology. The ANN studied in this work is based on the Multilayer Perceptron (MLP) architecture, whose learning phase uses the back-propagation technique [10–12]. To validate this work, simulations will be made on the structure of the obtained analog breast cancer classifier using the above-mentioned technology in order to compare the obtained results with those found in the state of the art [7, 13–18].

Within this work, the use of feed-forward architecture is fundamental. Information flows in a unidirectional manner from input to output layers [19], allowing the model to capture, and analyze complex patterns and

Manuscript received April 25, 2024; revised June 6, 2024; accepted June 12, 2024.
*Corresponding author

features relevant to breast cancer detection. The MLP structure, known for its capability to handle intricate data relationships [20], is strategically applied to address challenges and opportunities inherent in precise breast cancer classification using analog neural networks.

Most ANNs used for tasks such as pattern recognition and medical diagnosis are digital, meaning they rely on discrete data and numerical precision [20]. In contrast, AANN utilizes continuous values, offering advantages in modeling biological phenomena and handling subtle variations. AANN excel due to their robustness against noise and parallel processing capabilities. Additionally, they are more energy-efficient and adaptable, offering high-speed computation and chip dimension reduction, aligning better with biological principles. Using AANN for medical diagnostics, especially in breast cancer detection context, is relatively uncommon, making the research innovative and pioneering. This approach opens up new possibilities for achieving real-time diagnosis.

Furthermore, the primary motive behind this research work is to enhance the early detection of breast cancer through the development of advanced computational methodologies. By leveraging an AANN tailored specifically for breast cancer detection, the research aims to achieve the ability to identify subtle indicators of malignancy at an earlier stage, potentially leading to improved patient outcomes and survival rates. The application of analog computing principles to the domain of medical analysis, particularly for breast cancer detection, seeks to optimize computational resources and potentially enable real-time diagnosis, which is critical for improving the accessibility of diagnostic procedures.

The methods presented in some previous studies reported in literature have the following limitations: fixed weights without on-chip learning and use of a common source amplifier as a non-linear function; use of a Metal Oxide Semiconductor Field-Effect Transistor (MOSFET) operating only in weak inversion, resulting in low time response; use of unconventional architecture; low noise immunity; low speed; high complexity of the proposed systems; and complex communication between modules with respect to the operations performed by each circuit.

This paper is organized as follows: a brief literature review is presented in Section II, followed by the mathematical background in Section III. Section IV highlights the AANN circuit design methodology used. Simulation results are presented in Section V. Section VI then focuses on the interpretation and validation of the obtained results. Finally, a brief conclusion and perspective for further studies are given in Section VII.

II. Literature Review

Studies in this area began to take shape in 2016, and a brief review will help facilitate an in-depth understanding of different methods deployed within this work. In 2016, Jouni *et al*. designed a low-complexity architecture for breast cancer classification by pattern recognition [21]. They also focused on determining the activation function that minimizes classification errors. In 2017, Hassan Jouni *et al*. designed a programmable signal generator to produce the desired input and output signals used to test breast cancer Integrated Circuits (ICs) [8]. These signals have amplitudes of 1 V and operate at frequencies up to 5 kHz. In 2018, Hassan Jouni *et al*. designed a multiplier, an activation function, and its derivative used in the realization of a feed-forward ANN based on the MLP with a backpropagation algorithm under MATLAB Simulink [9]. In 2019, Hassan Jouni *et al*. implemented in MATLAB Simulink an AANN for the detection and classification of breast cancer based on non-ideal blocks with a classification error of 2.6% [10, 11].

That same year, Akshay Jayaraj *et al*. designed a common source nonlinear function that consists of an NMOS transistor coupled to a PMOS transistor [13]. To this day, this nonlinear function is the most commonly used activation function in AANN. In 2020, Sanjeev T. *et al*. proposed a fully integrated AANN based on the common source amplifier for breast cancer classification through a hardware-software co-design methodology with about 96.59% accuracy operating at 1.1 V [15]. In 2021, Alejandro Medina-Santiago *et al*. proposed a CMOS implementation of an AANN based on the optimization of an N-dimensional objective function having a 5-3-1 configuration architecture with a total power consumption of 46.08 mW [14]. In the same light, Gencer *et al*. proposed a paper focusing on the design and validation of an AANN [22]. In their work, basic building blocks of the AANN were constructed in UMC 90 nm technology, revealing that the AANN operates with a performance accuracy of 99.85% on the XOR gate.

Additionally, Freeman *et al*. [23] reviewed the use of ANNs for detecting breast cancer across various imaging techniques, highlighting accuracy improvements and screening advancements. Mina *et al*. [24] reviewed machine learning techniques, shedding light on automation strategies particularly relevant to circuit design. Houssein *et al*. [25] proposed an optimized deep-learning architecture for breast cancer diagnosis, integrating an improved marine predator algorithm to enhance performance. Concurrently, Ye *et al*. [26] introduced a method of analog deep neural network noise injection, ensuring stable prediction results despite parameter perturbations, which is vital for safety-critical applications. Ben Ahmed *et al*. [27] presented a hybrid UNET model for early breast cancer detection through ultrasound image segmentation, showcasing novel approaches to diagnosis. Lastly, Moges *et al*. [28] conducted a comparative analysis of ANN and support vector regression (SVR) models in predicting spray drift, contributing to environmental science research.

Sedlakova *et al*. [29] suggested that digital methods in medical diagnostics enhance accuracy, but present complexity and high-cost challenges. In contrast, analog techniques are simpler, cost-effective and more reliable, yet face stability challenges. This work however captures complex non-linear relationships between input and output variables, enabling highly complex system modeling. Thereby, significantly improving accuracy, energy efficiency, and speed processing, making it worthy for breast cancer detection. Thus, potentially revolutionizing the field of medical diagnostics.

III. Mathematical Background

Gilbert cells are essential components in the architecture of AANNs due to their intrinsic ability to enable analog signal processing without the need for digitization [30]. This is achieved without necessitating the conversion of these signals into a digital format. The operational principle of Gilbert cells involves the generation of an output signal directly proportional to the product of two distinct input signals [31].

This cell is depicted in Fig. 1 [32], consisting of three differential pairs (M1-M2, M3-M4, and M5-M6). The inputs: V_{X+} is applied to the gates of M2 and M3, V_{X-} is applied to the gates of M1 and M4, V_{Y+} is applied to the gates of M6, and V_{Y-} is applied to the gates of M5 respectively. The outputs: (I_{O+} and I_{O-}) are taken from the collector pairs (M1, M3) for I_1, and (M2, M4) for I_2 respectively. Assuming all the transistors are biased in the saturation region, obeying the ideal square-law equation, sized and matched so that the transconductance parameters satisfy $k_1=k_2=k_3=k_4=k_a$ and $k_5=k_6=k_b$.

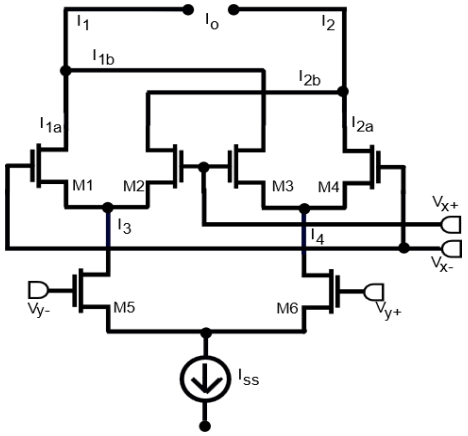

Fig. 1. MOS version of Gilbert cells [32].

Defining the output current I_O of Fig. 1 as $I_O=I_2-I_1=-(I_{2b}+I_{2a})-(I_{1a}+I_{1b})$, it can be shown that: $I_O=\sqrt{2k_a}V_X\left(\sqrt{I_3}\sqrt{1-\frac{k_aV_X^2}{2I_3}}-\sqrt{I_4}\sqrt{1-\frac{k_aV_X^2}{2I_4}}\right)$. If we demand $\frac{k_aV_X^2}{2I_3}<<1$ and $\frac{k_aV_X^2}{2I_4}<<1$, it follows that I_O depends linearly on V_X:

$$I_O=\sqrt{2k_a}\left(\sqrt{I_3}-\sqrt{I_4}\right)V_X$$

While the currents I_3, I_4 can be expressed by V_Y:

$$V_Y=\frac{1}{\sqrt{k_b}}\left(\sqrt{I_3}-\sqrt{I_4}\right)$$

Substituting V_Y into the expression of I_O, it follows that:

$$I_O=\sqrt{2k_ak_b}V_XV_Y \quad (1)$$

The output current in (1) yields an ideal analog multiplier. Notice that since both I_3, I_4 are I_{SS} and I_O dependents on both V_X and V_Y. Hence, V_X and V_Y must be kept small to maintain good linearity. This Gilbert cell structure will be used in this work for basic circuitries.

IV. Design of the Circuit Blocks

ANNs are most efficiently implemented using analog circuits [33]. Analog implementations are generally faster and require less hardware (fewer transistors) than digital VLSI implementations [4]. AVLSI implementations are parallel systems used in solving real-world problems [14], [34]. Multipliers and non-linear functions based on Gilbert cells are key elements in performing analog calculations efficiently [35]. Based on MLP architecture, each synapse needs a multiplier to multiply each input by the corresponding weight, and each neuron needs a nonlinear function and its derivative [7].

The feed-forward multipliers derived from the Gilbert cell will multiply the input, V_X by each corresponding synaptic weight, V_W to produce an output current, I_O as previously mentioned above. Unlike some neural networks that require an explicit adder block to combine weighted inputs, the Gilbert cell structure obviates this need. The current outputs from the hidden layer naturally sum up due to Kirchhoff's Current Law (KCL). Then the non-linear neural function will take the sum of all synapse multipliers connected to a neuron and produce an output. The output of the non-linear function will be the input of the derivative block for calculating the derivative of the non-linear function. As an example, the non-linear function can be the sigmoid (or logsigmoid) function [7].

It should be noted that an AANN system can contain thousands of multipliers and non-linear functions [36, 37]. It is crucial to optimize these analog circuit blocks to ensure precision, efficiency, and scalability. As a result, the surface area and the energy consumption of each block must be as low as possible. Based on the above statement, the methodology and design techniques of this work are initially based on the following six steps:

Step 1: Choosing the best circuit topology suited to our algorithm with respect to the state of the art.

Step 2: Dimensioning each basic block in order to optimize the specifications in terms of dynamics and precision.

Step 3: Choosing a low-cost and mature CMOS VLSI technology to achieve optimization at the transistor level.

Step 4: Using specialized and dedicated software to simulate and validate the main characteristics of the proposed circuits.

Step 5: Implementing a feed-forward AANN based on MLP architecture using an off-chip learning on-chip inference methodology.

Step 6: Simulating and testing the AANN performance on breast cancer classification in Cadence Virtuoso.

Incorporating an off-chip learning on-chip inference method enhances flexibility, performance, and ensures a reliable AANN implementation for medical diagnostics.

A. Multiplier Design

Multipliers are essential elements in analog signal processing, particularly in AVLSI implementations [38]. The design of this multiplier must take into account transistor biasing, linear or saturation regime, weak or

strong inversion, and threshold [7]. This section focuses on the design of a four-quadrant multiplier.

The main characteristics of a multiplier are its input and output dynamics, linearity, and bandwidth [39]. The design of an analog CMOS multiplier with high input dynamics and very low power consumption is proposed. One of the input voltages of this multiplier corresponds to the weight, V_W, used in the ANN algorithm for breast cancer detection and classification, meanwhile, the other input, V_{in}, corresponds to the biopsy cancer input [21]. The inputs of each multiplier are then chosen as voltages and the outputs as currents. The adder inputs will therefore be currents. This technique is deployed to eliminate the use of an analog adder in feed-forward propagation, thereby reducing the complexity of the overall network.

Moreover, the 9 attributes of the 699 biopsies correspond to voltages between 30 mV and 300 mV with a scale of 10 mV per coefficient (weight or input) [7]. Concerning the weight values, which are respectively between −1.37 and 1.17 in the hidden layer and between −3.54 and 3.48 in the output layer [21], the input dynamic of the multiplier is then imposed by the weights, which are higher than those of the attributes. The minimum and maximum weight values in the hidden and output layers vary between −3.54 and 3.48 for the logsigmoid activation function. The input dynamics of the analog CMOS multiplier are therefore −354 mV to 348 mV. Taking into account the input noise effects, this dynamic should increase up to 380 mV (or 400 mV). Besides, by applying a multiplying factor of 0.1 to the attributes instead of 0.3 as before, the input voltage dynamics of the analog multiplier will now correspond to:

- 10 mV to 100 mV for the first input, V_{in} and
- ±400 mV (or −354 mV to 348 mV without noise) for the second input, V_W.

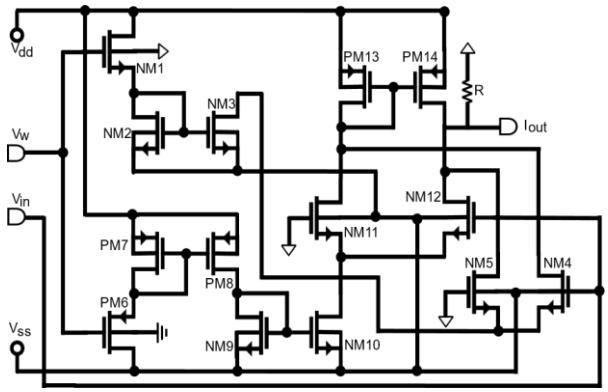

Fig. 2. Multiplier circuit.

Taking into account the considerations presented in the preceding paragraphs, we have the four-quadrant multiplier in Fig. 2.

To explain the behavior of the 4-quadrant multiplier, let us recall some transistor operation characteristics. A transistor does not move from its exponential behavior in weak inversion to its quadratic behavior in strong inversion; the transition is understood to be hybrid [7]. The boundaries between weak, moderate, and strong inversion remain complex, but can be approximated in terms of voltages or currents:

- $V_{GS} > V_T + 100$ mV for strong inversion;
- $V_T + 100$ mV $> V_{GS} > V_T - 100$ mV for moderate inversion;
- $V_{GS} < V_T - 100$ mV for weak inversion.

It is often preferable to design a circuit by defining the bias current. The following definitions can then be used to frame the limits of inversion:

- $I_O > 10I_S$ for strong inversion;
- $10I_O > I_O > 0.1I_S$ for moderate inversion;
- $I_O < 0.1I_S$ for weak inversion.

where I_S corresponds to the moderate reversal characteristic current and is defined by Eq. (2), in which W and L represent respectively the width and length of each transistor in Fig. 2.

$$I_S = \frac{2\mu C_{OX}}{K} U_T^2 \frac{W}{L} = \frac{2K_P}{K} U_T^2 \frac{W}{L} \tag{2}$$

with K_P and C_{OX} given by (3), and (4) respectively.

$$K_P = \mu C_{OX} \tag{3}$$

$$C_{OX} = \frac{\varepsilon_0 \varepsilon_r}{T_{OX}} = \frac{\varepsilon_{OX}}{T_{OX}} \tag{4}$$

With U_T=26 mV representing the thermal voltage, and defined by: $U_T = K_T/q$, K=0.7, ε_r = 3.9, ε_0 = 8.854×10^{-12} and μ represents the charge mobility.

Table I summarizes the Spice parameter characteristics of the transistors (nmos1v8 and pmos1v8) chosen from HCMOS9, a 90 nm CMOS technology from STMicroelectronics. The parameters provided include specifications on oxide thickness, oxide capacitance, charge mobility, and transconductance, essential for circuit simulation and analysis. Recalling permittivity:

$$\varepsilon_{OX} = \varepsilon_0 \varepsilon_r = 3.9 \times 8.854 \times 10^{-12} = 3.45 \times 10^{-11} \text{ F/m}$$

TABLE I: TRANSISTOR SPICE PARAMETERS

Spice parameters	NMOS	PMOS
T_{OX} (nm)	2.05	2.15
C_{OX} (F/m^2)	1.68×10^{-2}	1.60×10^{-2}
μ (m^2/Vs)	2.98×10^{-2}	6.27×10^{-2}
K_P (μA/V^2)	500.64	100.32

To limit the final consumption of the complete multiplier, a polarization current of the complete structure (presented in Fig. 2) is fixed at I_O=1 μA. For optimal operation of the corresponding transistors (differential pairs) in a strong inversion regime, the I_O>10I_S condition must be verified.

- For NMOS transistors, I_S can be fixed to: $I_{SN}=I_O/10$=1 μA/10=0.1 μA.

Considering Eq. (2), we obtained for the NMOS transistors:

$$I_{SN} = \frac{2K_{PN}}{K} U_T^2 \frac{W_N}{L_N} \tag{5}$$

$$\frac{W_N}{L_N} = 0.1034 \tag{6}$$

- For PMOS transistors, I_S can be fixed to: $I_{SP}=I_O/20=1\ \mu A/20=0.05\ \mu A$.

Considering Eq. (2), we obtained for the PMOS transistors:

$$I_{SP}=\frac{2K_{PP}}{K}U_T^2\frac{W_P}{L_P} \tag{7}$$

$$\frac{W_P}{L_P}=0.2580 \tag{8}$$

By taking into consideration the multiplier circuit presented in Fig. 2 and choosing W_N=120 nm, we obtain L_N=1.16 µm for transistors NM4, NM5, NM11, and NM12. By setting W_P=120 nm for PMOS transistors, we deduce L_P=465 nm for the transistors PM13 and PM14. The transistor sizing current generator is based on the following relationship: $I_O=V_{in}\sqrt{I_1}$, where I_1 follows a quadratic law according to the weight input, V_W. To size the transistors, we considered the maximum values of the inputs. Table II summarizes the dimensioning of the transistors in the complete multiplier circuit.

TABLE II: DIMENSIONS OF THE TRANSISTORS FOR THE MULTIPLIER

Transistor	Type	W/L (nm/µm)	Transistor	Type	W/L (nm/µm)
NM1	NMOS	150/10.0	PM8	PMOS	640/0.9
NM2	NMOS	150/1.55	NM9	NMOS	500/1.0
NM3	NMOS	580/6.0	NM10	NMOS	150/0.15
NM4	NMOS	120/1.16	NM11	NMOS	120/1.16
NM5	NMOS	120/1.16	NM12	NMOS	120/1.16
PM6	PMOS	180/3.0	PM13	PMOS	120/0.465
PM7	PMOS	500/0.51	PM14	PMOS	120/0.465

B. Linear Current to Voltage Converter Design

Before defining the AANN topology, the design of a linear current-to-voltage converter is needed. This section is dedicated to this purpose with transistors biased in weak inversion. This method makes it possible to obtain a significant gain with low power consumption, and easily realize a logsigmoid function between the output of the multiplier and the input of the chosen activation function.

K. Bult and H. Wallinga [40] proposed a linear current-to-voltage converter that has only two transistors. The two NMOS transistors, NM1 and NM2, both functioning in a biased saturation regime. To eliminate the body effect on the threshold voltage, V_{TH}, the gate of the two transistors is connected to their sources, as shown in Fig. 3.

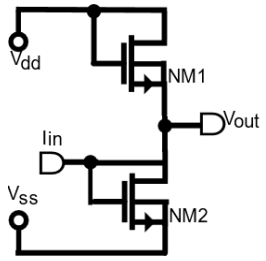

Fig. 3. Linear current to voltage converter circuit.

Taking $W_1=W_2=W$ and $L_1=L_2=L$, we have the following:

$$\beta=\frac{1}{2}KP_N\frac{W}{L} \tag{9}$$

$V_{GS1}=V_{OUT}-V_{SS}$ and $V_{GS2}=V_{DD}-V_{OUT}$

$$I_1=\beta\left(V_{OUT}-V_{SS}-V_{TH}\right)^2 \tag{10}$$

$$I_2=\beta\left(V_{DD}-V_{OUT}-V_{TH}\right)^2 \tag{11}$$

From KCL, $I_{IN}=I_1-I_2$, so I_{IN} can be written by taking the difference between (10) and (11) as in (12).

$$I_{IN}=\beta\left(V_{DD}-V_{SS}-2V_{TH}\right)\left(2V_{OUT}-V_{SS}-V_{DD}\right) \tag{12}$$

Knowing that $V_{SS}=-V_{DD}$, we deduce the output voltage, V_{OUT} as a function of the input current I_{IN} as in (13).

$$V_{OUT}=\frac{I_{IN}}{4\beta\left(V_{DD}-V_{TH}\right)} \tag{13}$$

We obtained the width and length (W/L) of NM1 and NM2 in Fig. 3 to be 150 nm and 950 nm, respectively.

C. Logsigmoid Type Activation Function Design

Feed-forward network responses are usually nonlinear functions that are achieved by summing the output currents of the synapses at each node. These functions are realized by the activation function circuit. More still, the derivative of the nonlinear function with respect to the weighted input is required for a fully analog on-chip learning neural using the backpropagation algorithm [37].

In this work, we utilize the sigmoid activation function [12], which consists of two linear current-to-voltage (IV) converters and a nonlinear function circuit. These IV converters transform input and output currents into corresponding input and output voltages as depicted in Fig. 4 and governed by Eq. (14).

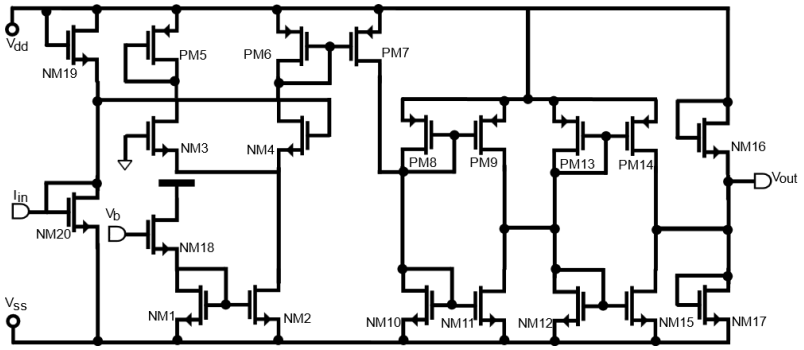

Fig. 4. Logsigmoid type activation function circuit.

$$V_{out} = \frac{1}{\left(1+e^{-V_{in}}\right)} \tag{14}$$

where V_{in} represents the input voltage of the logsigmoid activation function circuit obtained at the output of the linear current to voltage converter located at the input of Fig. 4.

$$V_{OUT(IV\text{-}converter)} = V_{in(logsig)} = \frac{I_{IN}}{4\beta\left(V_{DD}-V_{TH}\right)}$$

This function is equally approximated using transistors and has the same working principle as that of the hyperbolic tangent activation function [7]. Table III summarizes the dimensions of the transistors used in the circuit shown in Fig. 4.

TABLE III: DIMENSIONS OF THE TRANSISTORS FOR THE LOGSIGMOID TYPE ACTIVATION FUNCTION

Transistor	Type	W/L (nm/μm)	Transistor	Type	W/L (nm/μm)
NM1	NMOS	240/5.4	NM11	NMOS	150/1.5
NM2	NMOS	275/6.2	NM12	NMOS	150/1.5
NM3	NMOS	250/6.0	PM13	PMOS	1000/1.0
NM4	NMOS	280/5.1	PM14	PMOS	1000/1.1
PM5	PMOS	300/2.0	NM15	NMOS	150/1.5
PM6	PMOS	300/2.0	NM16	NMOS	150/1.1
PM7	PMOS	600/1.6	NM17	NMOS	150/1.1
PM8	PMOS	1000/1.0	NM18	NMOS	230/6.0
PM9	PMOS	1000/1.1	NM19	NMOS	150/10.0
NM10	NMOS	150/1.5	NM20	NMOS	150/10.0

D. Feed-Forward Analog Neural Network Layers Design

In the literature, several ANN learning techniques have been proposed to find an accurate weight set [41–43]. In this work, the gradient descent backpropagation algorithm is selected to train the neural network [44, 45]. Since the proposed ANN topology has no constraints on the learning performance, the chosen algorithm provides a simple and efficient implementation. The algorithm is developed in the MATLAB environment, and the input parameters are extracted from circuit simulations of the designed AANN. The system is fully automated, and all simulations can be performed in Cadence. Fig. 5 shows the implemented process steps.

Furthermore, the procedure starts by creating weight files for the ANN system to operate correctly. Afterward, a random set of weights is sent to the circuit simulator to find the output values corresponding to that weight set. Simulation outcomes are then transmitted to the algorithm, which then calculates the error between the actual sample outputs and the AANN results.

Also, the stochastic gradient descent method is used to compute the derivative of the mean squared error (SSE) function, which is used as the cost function [46, 47]. If all outputs produced by the AANN for each sample satisfy the desired tolerance criteria, the program stops the learning process with the last weight set. If the error is greater than the tolerance, the backpropagation algorithm attempts to minimize SSE. In particular, the change in each weight is estimated by calculating the derivative of the cost function for the corresponding weight. Consequently, the derivative of the logsigmoid plays a central role. The derivative of the activation function from the output curve of the logsigmoid circuit is calculated by the numerical finite difference method. After finding the change in each weight, the program updates the weight file. Subsequently, the circuit simulation is performed again with the newly calculated weights, as illustrated in Fig. 5. The flowchart loop runs until the tolerance criterion is reached, or the maximum iteration number is exceeded.

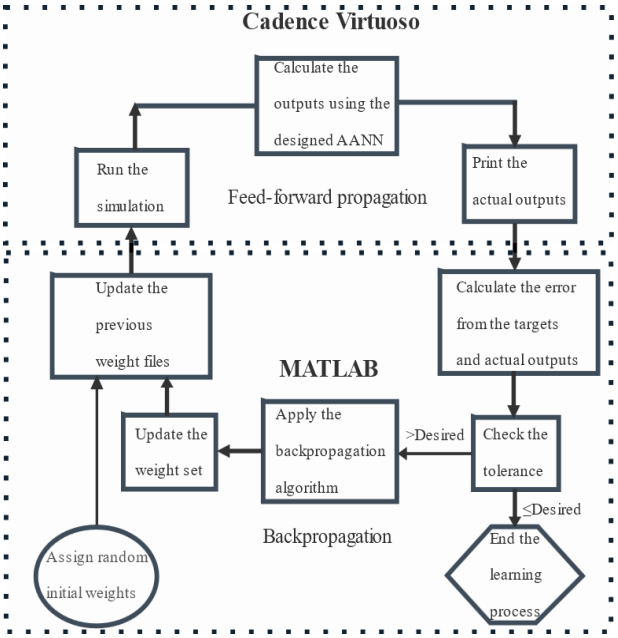

Fig. 5. 9-10-2 analog network training flowchart.

In addition, Fig. 6 shows the architectural layout of the proposed fully integrated off-chip learning on-chip inference feed-forward AANN implemented using analog circuits comprising logsigmoid activation functions and four-quadrant multipliers designed in 90 nm CMOS technology. This CMOS implementation can be considered as multi-layer, fully connected AANN that consists of an input layer, a hidden layer, and an output layer, as modeled by (15) and (16). The input layer of this breast cancer classifier comprises nine inputs corresponding to the attributes of the database. The hidden layer contains ten neurons, which apply nonlinear transformations to the inputs. The output layer consists of two neurons, which correspond to the output of the network. The outputs are classified as either benign (class 1: 01 in binary) or malignant (class 2: 10 in binary).

$$a_j = g_j\left(\sum_{i=1}^{9} w_{i,j}x_i\right); j = 1,2,...,10 \tag{15}$$

$$s_k = g_k\left(\sum_{j=1}^{10} w_{j,k}a_j\right); k = 1,2 \tag{16}$$

where: x_i are the inputs (the 9 cancer attributes of the Wisconsin Data Base), $w_{i,j}$ represents the 90 weight coefficients in the hidden layer, a_j corresponds to the 10 outputs of the hidden layer, $w_{i,j}$ represents the 20 weight coefficients in the output layer, and s_k corresponds to the 2 neurons at the outputs of the network. The activation function (g_j and g_k) of the layers is the logsigmoid, as earlier mentioned.

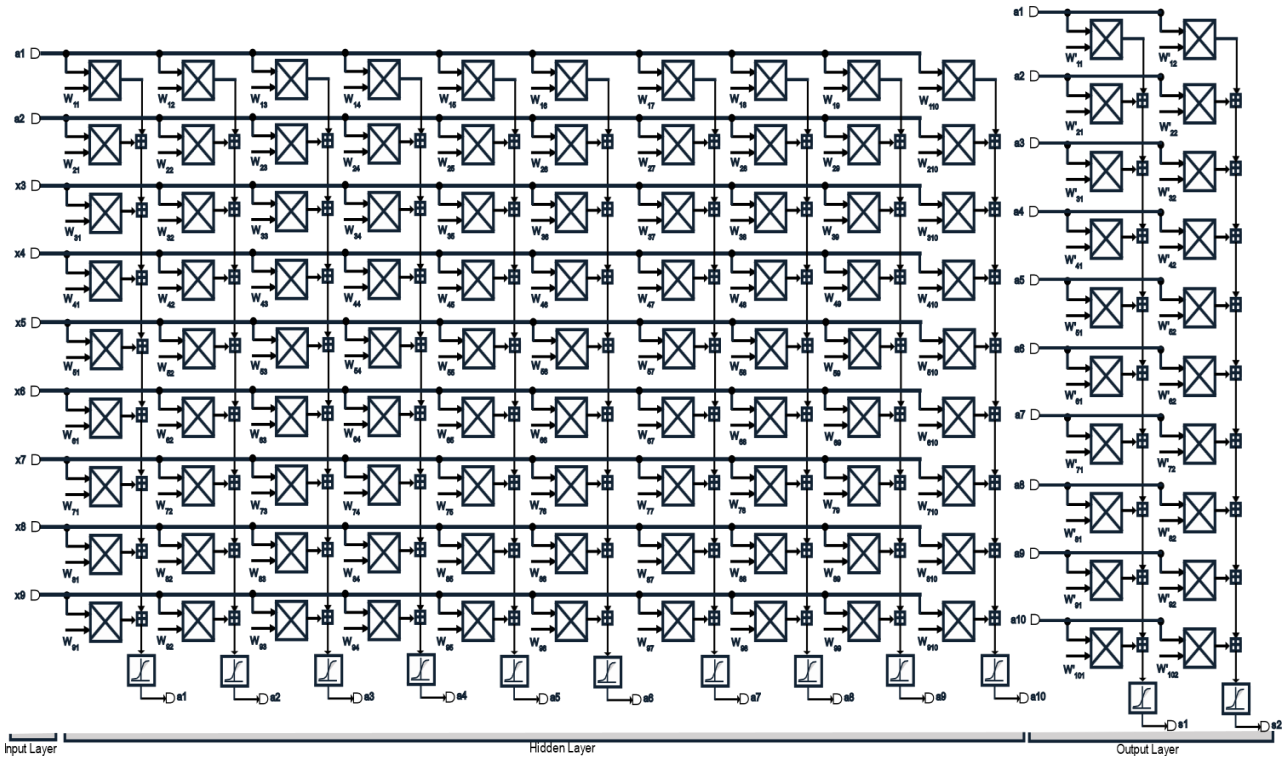

Fig. 6. 9-10-2 analog network circuit block diagram.

Off-chip learning is utilized in this work for several reasons. To begin with, it allows rapid training processes. Additionally, it saves much silicon area as the circuits dedicated to learning are not needed [48]. Moreover, off-chip learning works with chip-in-the-loop learning, which helps to address the mismatch between the network's behavioral model and the analog implemented circuit. As a result, any flaws in the hardware chip can be accounted for during the training stage, allowing for the updating of weights accordingly. This work is designed to facilitate efficient signal processing, learning, and decision-making using CMOS circuitries sized and optimized at the transistor levels for breast cancer diagnosis.

V. Simulation Results

A. Multiplier

1) Direct Current (DC) response analysis

The designed multiplier offers a linear output current *I*out with respect to the input voltage V_{in} ranging from −360 mV to 360 mV. Thus, respecting the Wisconsin cancer input attribute specification dynamics as earlier mentioned, which range from −100 mV to 100 mV. This input corresponds to the nine attributes of the Wisconsin database, whose values are from 1 to 10, with 1 corresponding to a voltage of 10 mV and 10 corresponding to a voltage of 100 mV. This first input dynamic is sufficient for breast cancer applications, and its DC simulation response is shown in Fig. 7.

The second input of the designed multiplier corresponds to the weights of each neuron. This value must be converted as a function of the square of the drain current to have a linear relationship with the output of the multiplier. The corresponding DC simulation response is shown in Fig. 8. This result shows a linearity range from −360 mV to 360 mV, which equally respects the weight specifications. In conclusion, this second multiplier input can be used as the weighted input for breast cancer applications.

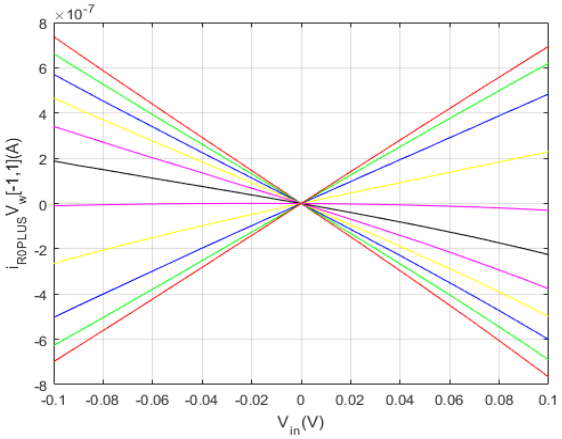

Fig. 7. I_{out} in function of V_{in} for different values of V_W.

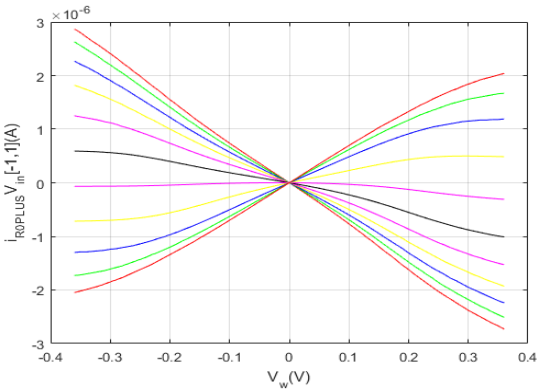

Fig. 8. I_{out} in function of V_W for different values of V_{in}.

Fig. 7 and Fig. 8 allow validation of the input dynamics considerations of the multiplier in DC domain used for AANN dedicated to the classification of breast cancer cells.

2) Transient response analysis

The transient response is presented for two different configurations with a maximum dynamic input voltage. In the first configuration shown in Fig. 9, the cancer input attribute voltage, V_{in} represented by the green sine wave, has a frequency of 100 Hz with an amplitude of 100 mV, and the weight input, V_W represented by the blue sine wave, has a frequency of 1 kHz with an amplitude of 1 V, producing an output amplitude modulated current signal represented in red.

In the second configuration shown in Fig. 10, the frequencies of both inputs are interchanged (that is, 1 kHz for V_{in} and 100 Hz for V_W) which equally produces an output amplitude modulated current signal of the same amplitude and frequency as in Fig. 9.

The spectrum of the output amplitude modulated current signals, I_{out} is calculated to confirm the transient analysis of the multiplier for the two configurations. The results for the two configurations are substantially identical and presented in Fig.11.

As expected, we obtain two lines at 0.9 kHz and 1.1 kHz which correspond to the mixtures of the two input signals at 100 Hz and 1 kHz. Their amplitude in both cases is about −130 dB. Harmonics due to non-linearities of the multiplier remain below −160 dB, which gives a noise margin of about 30 dB. This value is again largely sufficient for breast cancer applications.

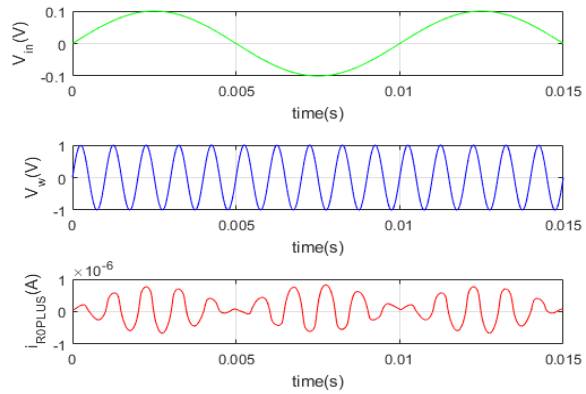

Fig. 9. Transient output I_{out} (weighted output in red) for V_{in} (input of a layer in green) at 100 Hz and V_W (weight coefficient in blue) at 1 kHz.

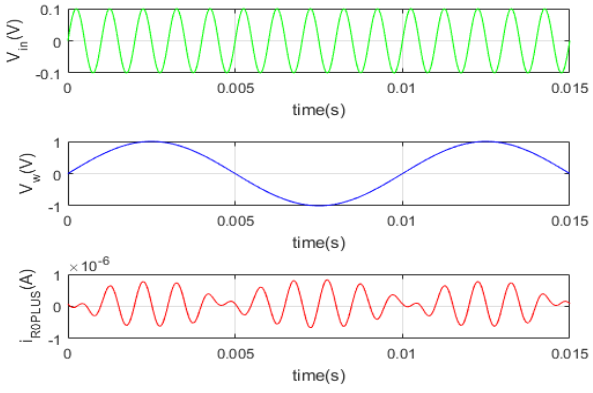

Fig. 10. Transient output I_{out} (weighted output in red) for V_{in} (input of a layer in green) at 1 kHz and V_W (weight coefficient in blue) at 100 Hz.

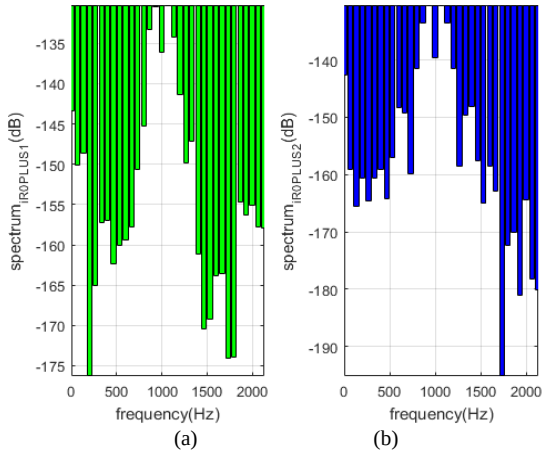

Fig. 11. I_{out} Spectra: configuration 1 (in green) and configuration 2 (in blue): (a) I_{out} spectrum for V_{in} at 100 Hz and V_W at 1 kHz and (b) I_{out} spectrum for V_{in} at 1 kHz and V_W at 100 Hz.

The various extensive transient simulation results conclusively demonstrate that the power consumption of the multiplier remains comfortably well below the threshold, with a maximum value not surpassing 3 µW (actually about 2.9 µW). This efficiency ensures that the multiplier operates within the desired power constraints.

B. Linear Current to Voltage converter

1) DC response analysis

To be compatible with the multiplier results presented in the previous section, the input dynamic I_{IN} is dimensioned in the range of [−5, +5] µA which is actually enough for the breast cancer diagnostic specifications as presented in Fig. 12 (a).

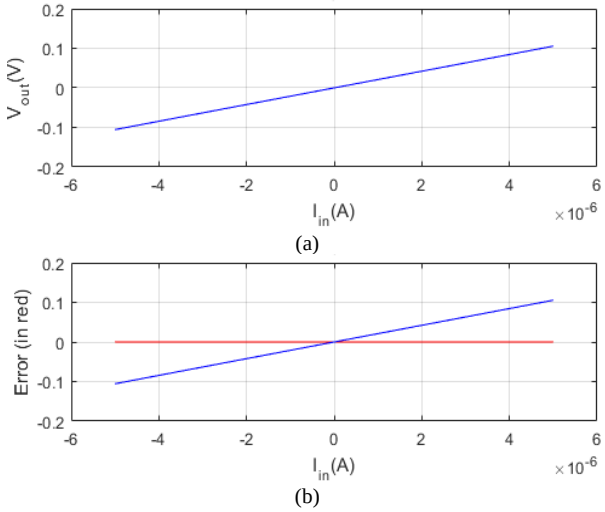

Fig. 12. Linear current to voltage converter DC response: (a) V_{out} in function of I_{IN} (in green) and (b) Error estimation between V_{out} and I_{IN} (in red).

This converter produces an output (colored in blue) that is directly proportional to the applied input, resulting in a variation of the output voltage, V_{out}, in the range [−100, +100] mV, with the error estimation between the input and output shown in red in Fig. 12 (b).

2) Transient response analysis

This section focuses on the transient response verification of the designed linear current-to-voltage

converter, which permits the validation of its study with respect to the feed-forward AANN conceptual framework as shown in Fig. 13 (a).

The input current is illustrated by a sine wave of amplitude 5 µA and frequency 1 kHz which produces a sine wave output voltage of amplitude 100 mV and frequency 1 kHz with no phase shift as depicted in Fig. 13 (c). This leads to the validation of the proposed linear current-to-voltage converter since the spectrums of the input and output signals respectively shown in Fig. 13 (b) and Fig. 13 (d) have similar shapes, with no time shift.

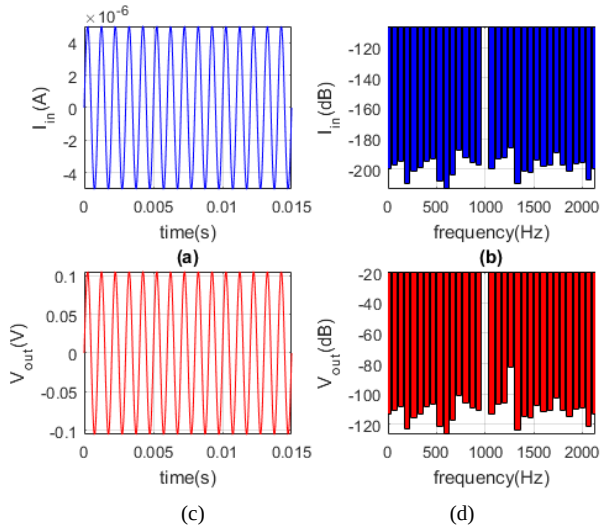

(c) (d)

Fig. 13. Linear current to voltage converter transient and spectrum responses: (a) Linear current to voltage converter transient input signal, (b) Linear current to voltage converter input signal spectrum of (a), (c) Linear current to voltage converter transient response, and (d) Linear current to voltage converter spectrum response of (c).

C. Logsigmoid Activation Function

1) DC response analysis

The output dynamics of the logsigmoid activation function are shown in Fig. 14. It is observed from the figure that the output voltage varies from 0 to 100 mV. The first configuration (Fig. 14 (a)) shows the output response for different biasing voltages, V_b ranging from 0 to 1 V with a step of 0.1 V. This output voltage will be used as the input voltage to the nonlinear derivative circuit.

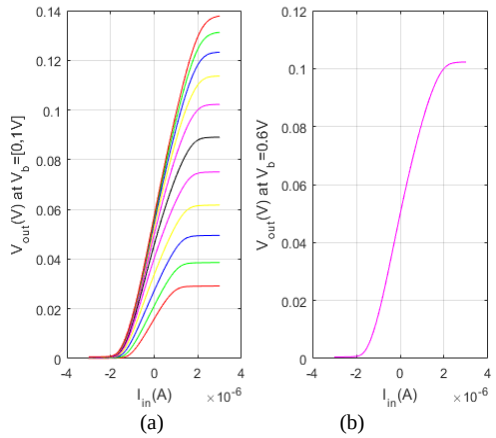

(a) (b)

Fig. 14. Logsigmoid type activation function DC response: (a) DC response for V_b ranging from 0 to 1 V and (b) DC response for V_b at 0.6 V.

The input dynamic is strictly respected since saturation of the output voltage is obtained at 0 mV and 100 mV before the extreme input current values. For V_b = 0.6 V, saturation is reached at I_{IN} = ±2 µA, as seen in Fig. 14 (b). The asymmetry observed corresponds to a value of 0 mV at I_{IN} = −2 µA, and 100 mV at I_{IN} = +2 µA, as required. This leads to the validation of the conceptual framework of the designed logsigmoid activation function in the DC domain.

2) Transient response analysis

The transient response of the logsigmoid-type activation function is presented in Fig. 15 (a). The input current is represented by a sine wave of amplitude 5 µA and a frequency of 1 kHz, which produces a square wave output voltage of amplitude 100 mV (which is the ideal amplitude value) and a fundamental frequency of 1 kHz with no phase shift, as illustrated in Fig. 15 (c). The spectrums of the input and output signals respectively shown in Fig. 15 (b) and Fig. 15 (d) have similar shapes.

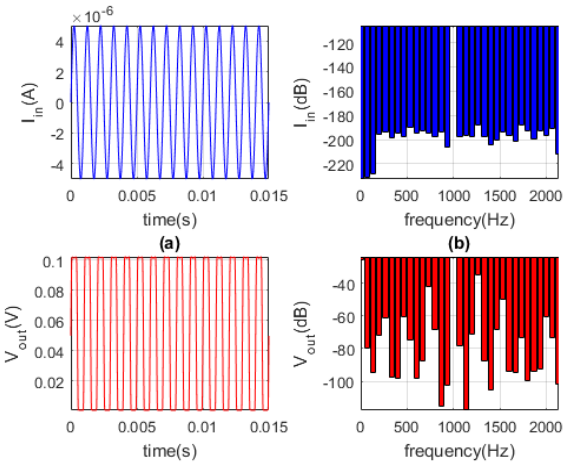

(c) (d)

Fig. 15. Logsigmoid type activation function transient response: (a) Logsigmoid transient input signal, (b) Logsigmoid input signal spectrum of (a), (c) Logsigmoid transient response, and (d) Logsigmoid spectrum response of (c).

D. Breast Cancer Software Classification

This work uses the supervised learning classification approach. Two types of neural networks are used in this work to classify cancer tumors, namely, feed-forward and backpropagation neural networks [49]. The classification process is divided into a training phase and a test phase. The neural network trains through the adjustment of the weights to predict the correct class. The desired output is specified as class one (01) for benign and class two (10) for malignant. This process is done through the use of the backpropagation algorithm. After the training phase is completed, the stored weights are then used in a feed-forward architecture for the neural network test phase.

The primary objective of this section is to provide the results of breast cancer training. MATLAB serves as a powerful and functional software environment for constructing or facilitates the creation and simulation of neural networks through coding [50]. Specifically, we focus on training our neural network for breast cancer detection. The algorithm parameters include a learning

rate of 0.295 and 1000 iterations. Fig. 16 (a) and Fig. 16 (b) show the performance and error measures, respectively. It is observed from Fig. 16 that the training of the network runs until the tolerance criterion is reached at the maximum iteration number. This criterion helps prevent overfitting by stopping the training process before the model becomes too tailored to the data.

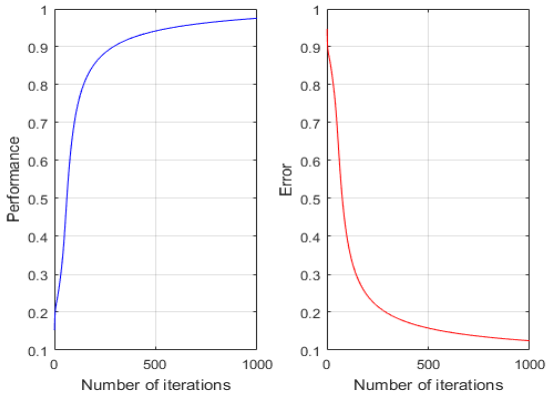

(a) (b)

Fig. 16. Neural network test phase software simulation curves: (a) Neural network performance curve and (b) Neural network error curve.

E. Monte Carlo and Process Corner simulation

AANNs are subject to process variations that vary the values and the characteristics of the circuit components. Small deviations may result in acquiring erroneous outputs, thereby leading to a larger error [51]. Taking into account the impact of these variations, the designed AANN is analyzed through Monte Carlo sensitive analysis and process corner variations. To perform the process corner analysis, we simulated five different corners based on the manufacturing variations of NMOS and PMOS devices: typical (tt), fast-fast (ff), slow-slow (ss), slow-fast (snfp), and fast-slow (fnsp). Fig. 17 to Fig. 19 show the histograms of logic 1 (in red) and logic 0 (in blue) values obtained from the Monte Carlo simulation of the cancer attribute samples for each corner.

The attributes from the Wisconsin database are translated in the form of voltages between 10 mV and 100 mV to perform the simulation in Cadence Virtuoso. These voltages are used as inputs to the designed AANN for simulation of the 699 biopsies.

Fig. 17 illustrates the DC response simulation results of ten different biopsies in which the first (Fig. 17 (a)) and second (Fig. 17 (b)) configurations correspond respectively to the first (represented by the colored blue histogram) and second (represented by the colored red histogram) neuron outputs of the output layer. These biopsies correspond to the benign class (01 in binary).

On the other hand, Fig. 18 illustrates the DC response results of ten other different biopsies, in which the first (represented by the colored red histogram, Fig. 18 (a)) and second (represented by the colored blue histogram, Fig. 18 (a)) configurations correspond respectively to the first and second neuron in the output layer. These biopsies reveal them to be malignant (10 in binary, corresponding respectively to a 1 for the first neuron and to a 0 for the second neuron of the output layer).

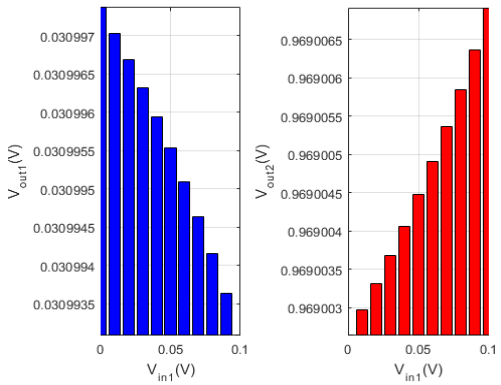

(a) (b)

Fig. 17. Feed-forward AANN DC response for ten benign samples: (a) First neuron output and (b) Second neuron output.

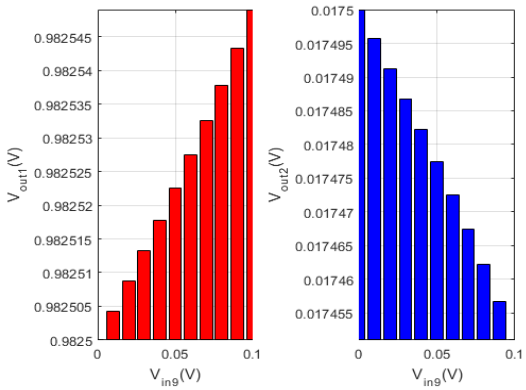

(a) (b)

Fig. 18. Feed forward AANN DC response for ten malignant samples: (a) First neuron output and (b) Second neuron output.

Similarly, Fig. 19 illustrates the DC response results of twenty close neuron outputs, of which ten are classified as benign-class tumors. That is, Fig. 19 (a) and Fig. 19 (b). The other ten are classified as malignant-class tumors. That is, Fig. 19 (c) and Fig. 19 (d). Despite the similarity of the two neuron outputs from these twenty biopsies, the classification task is successfully accomplished. This demonstrates the reliability of the design analog network as an ANN system for classification purposes.

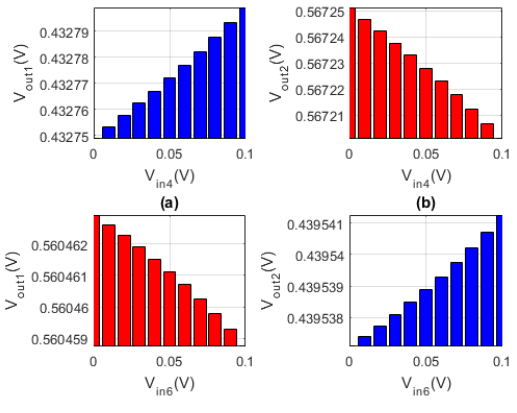

(c) (d)

Fig. 19. AANN DC response for ten close benign and ten close malignant neuron outputs: (a) First neuron output for ten close benign outputs, (b) Second neuron output for ten close benign outputs, (c) First neuron output for ten close malignant outputs, and (d) Second neuron output for ten close malignant outputs.

TABLE IV: PROCESS CORNER ANALYSIS RESULTS

Case	tt	ss	snfp	fnsp	ff
Logic 1	1.645	1.523	1.438	1.469	1.417
Logic 0	363.7	375.9	389.0	369.7	399.1

The process corner analysis shown in Table IV verifies that the output logic values are similar to the results obtained by using the typical (tt) process corner of transistors. Moreover, it is evident that the logic 1 limit is lower and the logic 0 limit is higher for the ff process corner. These minor changes can be effectively adjusted by retraining the weights using the backpropagation algorithm. Therefore, a new weight set that aligns better with the observed results of the AANN to the design specifications can be obtained. Thus, it can be inferred that AANNs can withstand manufacturing errors and quickly adapt to new situations.

The power supply rail of each analog circuit and computing hardware used for the implementation of this AANN is ±900 mV. Given the analog nature of this neural network, the circuits require specific voltage levels, which include positive and negative supply voltages, to ensure proper biasing and operation of analog circuits, leading to accurate analog computation. The power consumption of the analog neural network is shown in Fig. 20. It is known that the total power consumption of a circuit is obtained by calculating the area under the graph. Thus, the total power consumption of this AANN is 31.95 µW. The total elapsed time for the simulation of a sample in Cadence virtuoso is revealed from its "psf/spec." file to be 28.9595 s with a peak resident memory used of 68.7 Mbytes, yielding a total energy of 0.93 mJ. This very low power consumption is crucial for ensuring energy efficiency and minimizing heat dissipation. Hence, it could potentially contribute to a cost-effective, sustainable, and widely accessible diagnostic solution for breast cancer.

Fig. 21 illustrates the two outputs neuron prediction curve for the initial 50 biopsies samples of the analog implementation. The target output is elegantly depicted by the bold red curve, while the analog output gracefully follows the blue curve. These curves encapsulate the intricate dance of computation and representation within the neural substrate. This allows efficient and powerful data representation using less power.

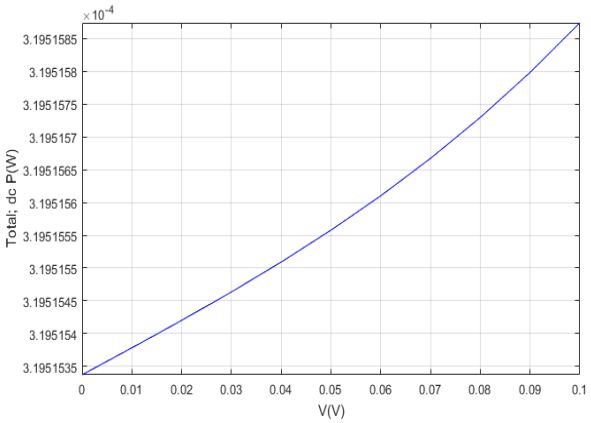

Fig. 20. Power consumption of the AANN.

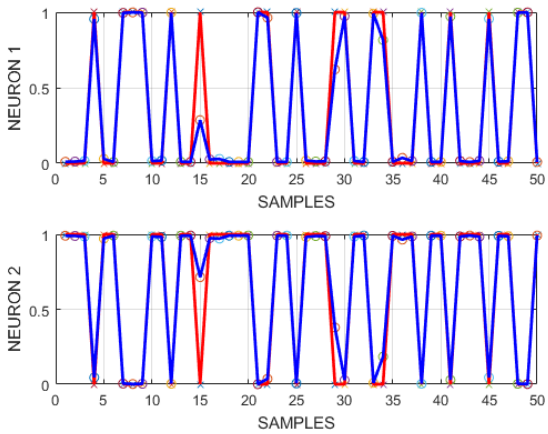

Fig. 21. Output prediction curves, with target in red and output in blue.

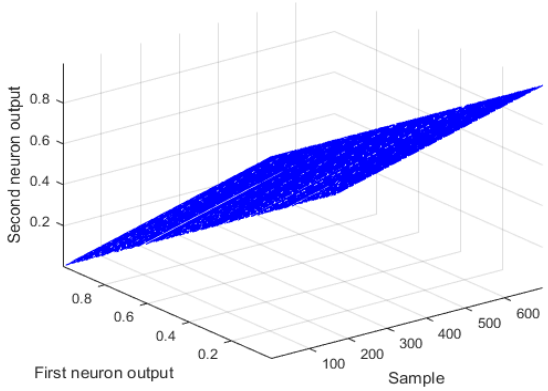

(a)

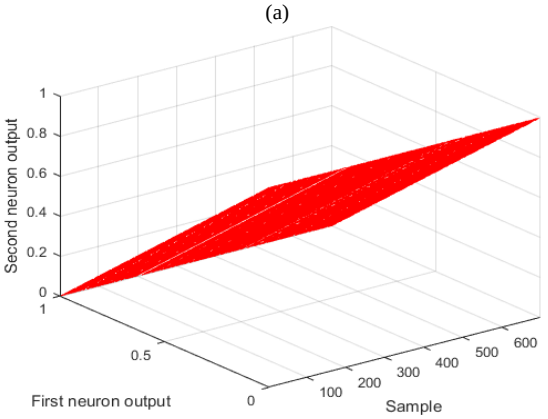

(b)

Fig. 22. AANN circular propeller: (a) Analog circular propeller (in blue) and (b) Target circular propeller (in red).

Furthermore, Fig. 22 depicts the circular propeller of the AANN breast cancer classifier. Fig. 22(a) and Fig. 22(b) represent respectively the analog (in blue) and target (in red) circular propellers. The uniform surface texture and consistent behavior across various regions suggest strong generalization capabilities and a well-fitted model. Implying the model effectively captures underlying data patterns and provides stable, reliable, and robust predictions.

The results of this section are used to conclude on the proposed analog chip, which classifies breast cancer as either malignant or benign, offering promising advantages such as energy efficiency, low power consumption, real-time diagnosis, and potential hardware optimizations. However, this work equally faces

difficulties related to precision due to the complexity of the network and the need for interdisciplinary collaboration. The next section focuses on the discussion of the simulation results.

VI. Discussion

A. Interpretation of the Results

Several different measures are commonly used to assess the performance measures of a proposed method. These measures are calculated with the aid of True Positive (TP), False Positive (FP), True Negative (TN), and False Negative (FN) samples. The extracted confusion matrix used to detect cancerous and non-cancerous breast tumors is clearly shown in Table V.

Table V: AANN Network Confusion Matrix

Approach	AANN classification	
Output class	non-cancerous	cancerous
Benign	444 (TN)	14 (FN)
Malignant	8 (FP)	233 (TP)

The eight missed benign tumor diagnoses can lead to unnecessary patient anxiety, increased healthcare costs due to follow-up tests, and potential overdiagnosis. In contrast, the fourteen missed malignant tumor diagnoses pose a risk that could delay treatment, worsen patient outcomes, and potentially lead to suboptimal patient care.

Classification performance measures include sensitivity (SE), specificity (SP), accuracy (AC), and Mathew's correlation coefficient (MCC).

$$SE = \frac{TP}{TP + FN}$$

$$SP = \frac{TN}{TN + FP}$$

$$AC = \frac{TP + TN}{TP + TN + FN + FP}$$

$$MCC = \frac{(TP \times TN) - (FP \times FN)}{\sqrt{(TP + FP)(TP + FN)(TN + FP)(TN + FN)}}$$

Table VI: AANN Network Performance Measures

Approach	Number of cases	SE	SP	AC	MCC
AANN	699	0.9433	0.9823	0.9685	0.9309

The performance measures shown in Table VI reveal a 96.85% accuracy obtained from Monte Carlo simulation results (that is, 22 incorrect logic evaluations of the breast cancer classifier out of the 699 Wisconsin dataset). Table VI equally reveals that the classifier has the advantage of obtaining higher speed and density due to a higher specificity performance measure. In contrast, it turns to have slight stability challenges with temperature variations due to a sensitivity performance measure close to, but less than 0.95. Additionally, the AANN has a very high network performance, as highlighted by Mathew's correlation coefficient of 0.9309, which represents the measure of the difference between predicted (obtained) values and actual values (targets).

The AANN is trained on the Wisconsin dataset that includes women of all ages, and races, as well as those with various genetic risk factors. It classifies both early-stage and late-stage tumors, considering clinical imaging artifacts such as motion artifacts, superimposed breast tissue and dense breast tissue.

B. Validation of the Results

By firstly subjecting the AANN to Monte Carlo analysis for evaluating process variations by simulating 1000 iterations with normally distributed transistor parameters (10% standard deviation), it facilitated the quantification of uncertainties and risks influencing the network's output predictions, enabling the identification of critical parameters affecting classification. This validation effort not only underscored the model's robustness and responsiveness to input fluctuations but also provided crucial insights for performance optimization, thereby bolstering network's confidence accuracy and applicability in breast cancer diagnosis.

Secondly, subjecting the AANN to process corner variations for assessing extreme conditions by simulating at five process corners (tt, ff, ss, snfp, and fnsp), three temperatures (–40 ℃, 25 ℃, 125 ℃), and ±10% supply rail (± 900 mV), facilitated a thorough model's performance evaluation under diverse scenarios. This effort does not only underscored network's resilience and adaptability in environmental challenges but also provided pivotal guidance for further optimizing the model's performance, therefore instilling confidence in its applicability for reliable diagnostic in variable environmental contexts.

Thirdly, varying transistor parameters and supply voltage within a ±10% range revealed that the AANN is relatively insensitive to these variances. However, the AANN performance is slightly sensitive to temperature variations, with a 10% temperature increase leading to a less than 1% decrease in accuracy due to increased noise and leakage currents. Mitigation strategies include using temperature-compensated circuits, or training with data covering a wide temperature range to enhance robustness.

Furthermore, Table VII compares this work with existing studies. Breast cancer classification is mostly done by ANNs implemented on graphic processing units (GPU), which easily consume huge amounts of power.

Table VII: Comparison with the State of the Art

Author	AC (%)	Application	Method	Design layout	Supply rail	Power	Energy
M. Kanojia [52]	96.77	Breast Cancer	GPU	--	--	--	--
Hua *et al*. [14]	96.43	Breast Cancer	CMOS IC	5-3-1	±2.500 V	46.08 mW	--
Sanjeev T. *et al*. [15]	96.59	Breast Cancer	CMOS VLSI	9-5-1	±1.100 V	50.00 µW	1.60 mJ
This work	96.85	Breast Cancer	CMOS VLSI	9-10-2	±900 mV	31.95 µW	0.93 mJ

Unlike studies that focus on digital circuits, the proposed implemented CMOS circuit classifiers can be

used to achieve similar tasks. This innovative approach offers the potential for improved energy efficiency, faster computations, a lesser complexity network, and precise analog pattern recognition, marking a notable departure from digital-centric methodologies. This work bridges the gap between digital-centric methods and promising AANNs, leading to improvements in medical diagnostics tasks, which could have a profound impact on healthcare.

Moreover, this study addresses limitations identified in previous studies, such as unconventional architecture and low noise immunity. It captures complex non-linear relationships between input and output variables, enabling accurate modeling of complex systems.

The advantage of this work lies in its pioneering utilization of analog computing for medical diagnostics. This innovative approach offers a distinct edge in terms of energy efficiency, real-time processing, and potential for nuanced pattern recognition when compared to the digital-centric methods employed in related studies. By leveraging analog computing principles, this work holds promise of enhancing computational speed, potentially revolutionizing the medical diagnostic landscape. The unique capabilities of AANN, including its energy efficiency and potential for real-time diagnosis, mark a paradigm shift in the field, positioning this research at the forefront of cutting-edge advancements in medical diagnostics.

Finally, this AANN is a small compact portable energy-autonomous IC chip of a few dimensions associated with a digital-to-analog converter that can be used in laboratories to record breast cancer attributes and provide appropriate diagnostics. It serves as a diagnostic decision support system tool in the hospital which will help the clinicians and physicians in faster decision-making and by so doing, will ultimately reduce the risk of false diagnosis. Thus, hospitals will have to buy the AANN for utilization by physicians, thereby empowering physicians with a medical diagnostic cutting-edge tool.

VII. Conclusion

The design and implementation of an AANN for breast cancer cell classification as benign or malignant is presented in this paper. The MLP architecture with a back propagation algorithm was retained using MATLAB, featuring nine inputs, ten neurons in the hidden layer and two neurons in the output layer. Our main contribution was the development of novel analog circuits for AANN implementation. Verification and validation occurred in Cadence Virtuoso through Monte Carlo analysis and process corner variation analysis. The Spice simulation results aligned with work specifications, showing the final circuit operating at ± 900 mV power supply rail, consuming 31.95 µW. The "psf/spec." simulation time was 28.9595 seconds per sample, with a peak resident memory usage of 68.7 Mbytes, yielding a total energy of 0.93 mJ. The AANN achieved a 96.85% accuracy and 0.9309 MCC, promising for breast cancer classification.

This work holds the impact of providing a solid background for future studies, opens up new possibilities for optimizing computational resources and revolutionizing breast cancer screening, enabling faster diagnosis for timely treatment and improved patient outcomes, reducing healthcare costs, reducing disparities in breast cancer care, prioritizing investments in AANN research and development, and establishing policies that support the integration of AANNs into clinical practice.

However, implementing a fully integrated on-chip learning AANN based on MLP architecture with backpropagation can improve the reliability and efficiency of this work for breast cancer diagnosis.

Conflict of Interest

The authors declare no conflicts of interest.

Author Contributions

The primary investigators and lead authors of the study are Djimeli-Tsajio Alain B. and Koagne Longpa T. Silas. Djimeli-Tsajio Alain B. was responsible for the software specifications of the AANN, while Geh Wilson Ejuh played a key role in the AANN's mathematical modeling. Both served in a supervisory capacity. Additionally, expertise in the training process of the ANN network was provided by Lienou T. Jean-Pierre and Noulamo Thierry. The implementation and testing of the AANN for breast cancer diagnosis were carried out by Koagne Longpa T. Silas. All authors had approved the final version.

Data Availability Statement

Data supporting the findings of this study are available from the corresponding author upon reasonable request.

References

[1] R. Qamar and B. A. Zardari, "Artificial neural networks: An overview," *Mesopotamian Journal of Computer Science*, pp. 130–139, 2023. doi: 10.58496/MJCSC/2023/015

[2] M. Anguita, F. J. Pelayo, A. Prieto, and J. Ortega, "Analog CMOS implementation of a discrete time CNN with programmable cloning templates," *IEEE Trans. on Circuits and Systems II: Analog and Digital Signal Processing*, vol. 40, no. 3, pp. 215–218, 1993.

[3] H. Chible, M. E. H. Jouni, and B. Hassan-Beirut, "Analog multiplier for feed forward neural network signal processing," in *Proc. the 7Th Int. Conf. on Signal Processing, Pattern Recognition and Applications*, 2010. doi:10.2316/P.2010.678-053

[4] M. Fernando, A. Ana, and M. Alexandre, "Artificial neural networks: A review of commercial hardware," *Engineering Applications of Artificial Intelligence*, vol. 17, pp. 945–952, 2004. doi: 10.1016/j.engappai.2004.08.011

[5] M. Rizwan and Y. R. Alharbi, "Artificial intelligence-based approach for short term load forecasting for selected feeders at Madina Saudi Arabia," *International Journal of Electrical and Electronic Engineering & Telecommunications*, vol. 10, no. 5, pp. 300–306, 2021.

[6] A. Frank and A. Asuncion, *UCI Machine Learning Repository*, School of Information and Computer Science, University of California, 2010.

[7] H. Jouni, "Cellules analogiques CMOS pour réseaux de neurones. Application à la classification des cellules cancéreuses dans le sein," dissertation, COMUE Université Côte d'Azur, Lebanese International University, 2018.

[8] H. Jouni, A. Harb, G. Jacquemod, and Y. Leduc, "Programmable signal generator for neural network application," in *Proc. 2017 29th Int. Conf. on Microelectronics*, 2017. doi: 10.1109/ICM.2017.8268881

[9] H. Jouni, A. Harb, G. Jacquemod, and Y. Leduc, "Creation of real

blocks for neural network using Simulink," in *Proc. 2018 Int. Conf. on Computer and Applications*, 2018. doi: 10.1109/COMAPP.2018.8460327
[10] H. Jouni, A. Harb, G. Jacquemod *et al.*, "Design and specification of analog artificial neural network," *SN Applied Sciences*, vol. 1, no. 11, pp. 1–15, 2019. doi: 10.1007/s42452-019- 1243-4
[11] H. Jouni, A. Harb, G. Jacquemod, and Y. Leduc, "Design and specification of analog artificial neural network," *SN Applied Sciences*, vol. 1, no. 11, pp. 1–15, 2019.
[12] Z. Jia and B. Kim, "Online trained neural network-PI speed controller for DTC based IPMSM drives," *International Journal of Electrical and Electronic Engineering & Telecommunications*, vol. 7, no. 3, pp. 108–113, 2018.
[13] A. Jayaraj, I. Banerjee, and A. Sanyal, "Common-source amplifier based analog artificial neural network classifier," in *Proc. 2019 Int. Symp. on Circuits and Systems*, pp. 1–5, 2019. doi: 10.1109/ISCAS.2019.8702426
[14] M. S. Alejandro, C. A. Hernandez-Gracidas, L. A. Morales-Rosales, I. Algredo-Badillo, M. Amador Garcıa, and J. A. Orozco Torres, "CMOS implementation of ANNs based on analog optimization of n-dimensional objective functions," *Sensors*, vol. 21, no. 21, p. 7071, 2021.
[15] T. S. Chandrasekaran, R. Hua, I. Banerjee, and A. Sanyal, "A fully-integrated analog machine learning classifier for breast cancer classification," *Electronics*, vol. 9, no. 3, p. 515, 2020.
[16] A. Arabi, N. Bourouba, A. Belaout, and M. Ayad, "An accurate classifier based on adaptive neuro-fuzzy and features selection techniques for fault classification in analog circuits," *Integration*, vol. 64, 2019. doi: https://doi.org/10.1016/j.vlsi.2018.08.001
[17] B. Gao, Y. Zhou, Q. Zhang, S. Zhang, P. Yao, Y. Xi, Q. Liu, M. Zhao, W. Zhang, Z. Liu, X. Li, J. Tang, H. Qian, and H. Wu, "Memristor-based analogue computing for brain-inspired sound localization with in situ training," *Nature Communications*, vol. 13, no. 1, 2022. doi: https://doi.org/10.1038/s41467-022-29712-8
[18] W. Xu, J. Wang, and X. Yan, "Advances in memristor-based neural networks," *Frontiers in Nanotechnology*, vol. 3, 645995, 2021. doi: 10.3389/fnano.2021.645995
[19] N. Tran-Thi-Kim, T. Pham-Viet, I. Koo, V. Mariano, and T. Do-Hong, "Enhancing the classification accuracy of rice varieties by using convolutional neural networks," *International Journal of Electrical and Electronic Engineering & Telecommunications*, vol. 12, no. 2, pp. 150–160, 2023.
[20] M. Puttagunta and S. Ravi, "Medical image analysis based on deep learning approach," *Multimedia Tools and Applications*, vol. 80, pp. 24365–24398, 2021.
[21] H. Jouni, M. Issa, A. Harb, G. Jacquemod, and Y. Leduc, "Neural network architecture for breast cancer detection and classification," in *Proc. 2016 Int. Multidiscip. Conf. on Engineering Technology*, 2016, pp. 37–41.
[22] F. B. Gencer, X. Xhafa, B. B. İnam, and M. B. Yelten, "Design and validation of an artificial neural network based on analog circuits," *Analog Integrated Circuits and Signal Processing*, vol. 106, pp. 475–483, Marr. 2021.
[23] K. Freeman, J. Geppert, C. Stinton, D. Todkill, S. Johnson, A. Clarke, and S. Taylor-Phillips, "Use of artificial intelligence for image analysis in breast cancer screening programmes: Systematic review of test accuracy," *BMJ*, vol. 374, 2021. doi: https://doi.org/10.1136/bmj.n1872
[24] R. Mina, C. Jabbour, and G. E. Sakr, "A review of machine learning techniques in analog integrated circuit design automation," *Electronics*, vol. 11, no. 3, p. 435, 2022. doi: https://doi.org/10.3390/electronics11030435
[25] E. H. Houssein, M. M. Emam, and A. A. Ali, "An optimized deep learning architecture for breast cancer diagnosis based on improved marine predators' algorithm," *Neural Computing and Applications*, vol. 34, no. 20, pp. 18015–18033, 2022.
[26] N. Ye, L. Cao, L. Yang, Z. Zhang, Z. Fang, Q. Gu, and G. Yang, "Improving the robustness of analog deep neural networks through a bayes-optimized noise injection approach," *Communications Engineering*, vol. 2, no. 1, #25, 2023.
[27] I. B. Ahmed, W. Ouarda, and C. B. Amar, "Hybrid UNET model segmentation for an early breast cancer detection using ultrasound images," in *Proc. Int. Conf. on Computational Collective Intelligence*, 2022, pp. 464–476.
[28] G. Moges, K. McDonnell, M. A. Delele, A. N. Ali, and S. W. Fanta, "Development and comparative analysis of ANN and SVR-based models with conventional regression models for predicting spray drift," *Environmental Science and Pollution Research*, vol. 30, no. 8, pp. 21927–21944, 2023.
[29] J. Sedlakova, A. L. Westermair, N. Biller-Andorno, C. A. Meier, and M. Trachsel, "Comparison of analog and digital patient decision aids for the treatment of depression: A scoping review," *Frontiers in Digital Health*, vol. 5, #1208889, 2023.
[30] D. K. McNeill, C. R. Schneider, and H. C. Card, "Analog CMOS neural networks based on Gilbert multipliers with in-circuit learning," in *Proc. 36th Midwest Symp. on Circuits and System*, 1993, pp. 1271–1274.
[31] S. L. Pinjare, "Design and analog VLSI implementation of neural network architecture for signal processing," *European Journal of Scientific Research*, vol. 27, no. 2, pp 199–216, 2009.
[32] B. D. Yammenavar, V. R. Gurunaik, R. N. Bevinagidad, and V. U. Gandage, "Design and analog VLSI implementation of artificial neural network," *International Journal of Artificial Intelligence & Applications (IJAIA)*, vol. 2, no. 3, pp. 96–109, 2011.
[33] S. C. Liu, J. P. Strachan, and A. Basu, "Prospects for analog circuits in deep networks in analog circuits for machine learning, current/voltage/temperature sensors, and high-speed communication: Advances in analog circuit design," *Cham.*, pp. 49–61, 2021. doi: https://doi.org/10.1007/978-3-030-91741-8_4
[34] A. F. Murray, D. Del Corso, and L. Tarassenko, "Pulse-stream VLSI neural networks mixing analog and digital techniques," *IEEE Trans. on Neural Networks*, vol. 2, no. 2, pp. 193–204, 1991.
[35] W. P. Chen, T. Y. Wang, H. L. Xu, and X. W. Liu, "A four-quadrant analog multiplier based on CMOS source coupled pair," *Key Engineering Materials*, vol. 483, pp. 487–491, 2011. doi: 10.4028/www.scientific.net/KEM.483.487
[36] S. Panda, S. Srimani, B. Maji, and A. Mukhopadhysay, "High performance CMOS four quadrant analog multiplier in 45 nm technology," *International Journal of Application or Innovation in Engineering & Management*, vol. 2, pp. 1–7, 2013. doi: 10.1109/JSSC.1986.1052546
[37] S. L. Pinjare and P. C. P. Raj, "Design and analog VLSI implementation of neural network architecture for signal processing," *European Journal of Scientific Research*, vol. 27, no. 2, pp. 199–216, 2009.
[38] V. Nandhini and K. Sambath, "VLSI implementation of multiplier design using reversible logic gate," *Analog Integrated Circuits and Signal Processing*, vol. 115, no. 1, pp. 93–100, 2023.
[39] G. Han and E. Sanchez-Sinencio, "CMOS transconductance multipliers: A tutorial," *IEEE Trans. on Circuits and Systems II: Analog and Digital Signal Processing*, vol. 45, no. 12, pp. 1550–1563, 1998.
[40] R. Wojtyna and T. Talaska, "Transresistance CMOS neuron for adaptive neural networks implemented in hardware," *Bulletin of the Polish Academy of Sciences: Technical Sciences*, vol. 54, no. 4, pp. 443–448, 2006.
[41] Z. You and C. Lu, "A heuristic fault diagnosis approach for electro-hydraulic control system based on hybrid particle swarm optimization and Levenberg–Marquardt algorithm," *Journal of Ambient Intelligence and Humanized Computing*, pp. 1–10, 2018. doi: https://doi.org/ 10.1007/s12652-018-0962-5
[42] P. Zhou and J. Austin, "Learning criteria for training neural network classifiers," *Neural computing and applications*, vol. 7, pp. 334–342, 1998. doi: https://doi.org/10.1007/BF01428124
[43] J. Spiegel, P. Mueller, D. Blackman *et al.*, "An analog neural computer with modular architecture for real-time dynamic computations," *IEEE Journal of Solid-State Circuits*, vol. 27, no. 1, pp. 82–92, 1992
[44] MathWorks MATLAB and statistics toolbox release 2016a, The MathWorks Inc, Natick, Massachusetts, United States, 2016.
[45] C. Mead, "Neuromorphic electronic systems," in *Proc. the IEEE*, vol. 78, no. 10, pp. 1629–1636, 1990.
[46] G. I. Salama, M. Abdelhalim, and M. A. Zeid, "Breast cancer diagnosis on three different datasets using multi-classifiers," *International Journal of Computer and Information Technology*, vol. 1, no. 1, pp. 36–43, 2012.
[47] N. H. Serajee, S. Mannan, R. Abdulghafor, S. Wani, A. A. Ibrahim, and A. Olowolayemo, "Breast cancer prediction using machine learning," *International Journal on Perceptive and Cognitive Computing*, vol. 8, no. 1, pp. 24–28, 2022.
[48] M. F. Aslan, "A hybrid end-to-end learning approach for breast cancer diagnosis: Convolutional recurrent network," *Computers*

and Electrical Engineering, vol. 105, 108562, 2023. doi: https://doi.org/10.1016/j.compeleceng.2022.108562
[49] H. Hakkoum, A. Idri, and I. Abnane, "Assessing and comparing interpretability techniques for artificial neural networks breast cancer classification," *Computer Methods in Biomechanics and Biomedical Engineering: Imaging & Visualization*, vol. 9, no. 6, pp. 587–599, 2021.
[50] I. AlShourbaji, P. Kachare, W. Zogaan, L. J. Muhammad, and L. Abualigah, "Learning features using an optimized artificial neural network for breast cancer diagnosis," *SN Computer Science*, vol. 3, no. 3, 2022. doi: https://doi.org/10.1007/s42979-022-01129-6
[51] A. S. Orgenci, G. Dundar, and S. Balkur, "Fault-tolerant training of neural networks in the presence of MOS transistor mismatches," *IEEE Trans. on Circuits and Systems II: Analog and Digital Signal Processing*, vol. 48, no. 3, pp. 272–281, 2001
[52] M. Kanojia, "Malignancy detection in breast histo-images using multi-layer perceptron," in *Proc. Int. Conf. on Soft Computing and Pattern Recognition*, pp. 553–562, 2021.

Djimeli Tsajio Alain Bernard received a B.S. (2001) and M.S. with thesis (2004) from the Faculty of Science of the University of Yaoundé I and the Ph.D. (2016) from the Faculty of Science of the University of Dschang, all in Cameroon in the field of physics option Electronics. Since 2006, he has joined Fotso Victor University Institute of Technology of the University of Dschang as a lecturer in the Department of Telecommunication and Network Engineering. He is a member of UR.A.I.A. of the present university where he is carrying out research in the field of Artificial Intelligence for biomedical process. He is the author of more than 10 research papers.

Koagne Longpa T. Silas earned his Technical School Teacher's Training Diploma I (DIPET I) in Electrical and Electronics Engineering, option Electronics at the University of Bamenda in 2018. His unwavering commitment to academic excellence led him to obtain a Technical School Teacher's Training Diploma II (DIPET II) in Electrical and Electronics Engineering, option Electronics at the University of Bamenda in 2020. His deep-rooted passion for research in electrical and electronics engineering motivated him to further his studies at the University of Dschang where he obtained a bachelor's degree in sciences and technology (BSc) in physics, option Electrical, Electronics, and Automation (EEA) in 2021 and followed by a master degree of sciences and technology (MSc) in physics option Electrical, Electronics and Automation (EEA) in 2022. He currently stands at the forefront of technology and scientific research as a UR.A.I.A. member and Ph.D. Student in Physics specializing in Electronics at the University of Dschang.

Lienou T. Jean-Pierre, born in Kekem in 1966. After studying Russian language in 1988 at Kharkiv Polytechnic Institute, He obtained his MSc in systems and networks at Kyiv Polytechnic Institute of the National Technical University of Ukraine in 1994. After working sometimes in private companies mainly as Biomedical Engineer or System Engineer, He joined the teaching staff of the University of Dschang as Assistant Lecturer in 2002 and obtained his Ph.D. in 2015 at Yaoundé National Advanced School of Engineers of the University of Yaoundé I, Cameroon. He is now an associate professor of Computer Science and was posted as head of the Department of Computer Engineering in the College of Technology at the University of Bamenda in 2017. Author and co-author of publications in the area of method engineering, multi-agent systems, neural networks, and computer vision. The recent research interests concern both some open questions concerning cyber resilience and Machine Learning. He is a member of the International Association of Engineers. He received the first Cameroon National Prize of Innovation in Embedded Systems and is currently a peer reviewer in a few International Journal of Computer Science.

Noulamo Thierry earned his master's degree, Diploma of Advanced Studies (DEA), and Ph.D. in software engineering science from the University of Yaoundé I in 2000, 2001, and 2010, respectively. He is currently working as a lecturer in the Department of Computer Engineering at Fotso Victor University Institute of Technology (IUT-FV) of Bandjoun, since 2004. He has been a member of EANG since 2009, Life member of UR.A.I.A. since 2008. He has published more than 11 research papers in reputed international journals and conferences. His main research work focuses on Process Automation using MDE and Muti-Agent approach. He has 18 years of teaching experience and 11 years of research experience.

Geh Wilson Ejuh is a distinguished academic and researcher in the field of electrical and electronic engineering. He embarked on his academic journey at the University of Yaounde I, where he earned a BSc in physics-chemistry in 2003, followed by an MSc in physics with a focus on materials science in 2006. After working as a part-time lecturer in the Physics Department of ENS Bambili from 2007, his career as an educator began at Gombe State University in Nigeria, where he served as an Assistant Lecturer from November 2008. He then joined the teaching staff of IUT-FV Bandjoun, University of Dschang as an Assistant Lecturer in 2011, and obtained his PhD in 2013 in physics option materials sciences from the Faculty of Science of the University of Yaoundé 1, Cameroon. In 2014, he was promoted to the rank of Lecturer, in 2019 to the rank of Associate Professor and in 2023, he was promoted to the rank of Professor of Physics. He was posted as Head of Services for Teaching and Academic Activities in NAHPI in 2017 and in 2021 as Head of Services for continuous training in NAHPI, University of Bamenda. Currently, he contributes his expertise at the University of Dschang, IUT-FV Bandjoun, Cameroon, within the General and Scientific Studies department, and at the National Higher Polytechnic Institute of the University of Bamenda, in the Department of Electrical and Electronic Engineering. His research is at the forefront of exploring the electronic, optoelectronic, photonic, and thermodynamic properties of organic and pharmaceutical molecules. His work on the doping of fullerene and other organic materials is particularly notable. He established himself as an expert in Material Characterization, Optoelectronics, Photovoltaics, and Nanotechnology with a prolific output of 80 publications, which have garnered 16,782 reads and 741 citations. His contributions to the scientific community are substantial, standing at the head of the Quantum Dynamics Research Group (QDRG) at ICTP-EAIFR, and being a member of reviewer to many Journals. His dedication to advancing the field of materials science and engineering is evident in his impressive academic and research accomplishments.